nature communications

Article

https://doi.org/10.1038/s41467-025-59489-5

Fusogenic lipid nanoparticles for rapid delivery of large therapeutic molecules to exosomes

Received: 3 September 2024

Accepted: 25 April 2025

Published online: 23 May 2025

Check for updates

Gamsong Son[1,2,6], Jiyoung Song[3,6], Jae Chul Park[2], Hong Nam Kim[1,3,4,5] ✉ & Hojun Kim[1,2] ✉

Exosomes, as cell-derived lipid nanoparticles, are promising drug carriers because they can traverse challenging physiological barriers such as the blood-brain barrier (BBB). However, a major obstacle in utilizing exosomes as drug carriers is loading large therapeutic molecules without compromising the structural integrity of embedded biomolecules. Here, we introduce a membrane fusion method utilizing fusogenic lipid nanoparticles, cubosomes, to load large molecules into exosomes in a non-destructive manner. When the drug-loaded cubosome and exosome solutions are simply mixed, membrane fusion is completed in just 10 min. Our method effectively loads doxorubicin and immunoglobulin G into exosomes. Moreover, even the most challenging molecule—mRNA—is loaded with nearly 100% efficiency, demonstrating the versatility of our approach. In terms of biological behavior, the resulting hybrid exosomes preserve the functional behavior of exosomes in BBB uptake and penetration. Surprisingly, controlling exosome-to-cubosome ratios allows precise control over BBB uptake and transport. Furthermore, these hybrid exosomes retain cell-specific delivery properties, preserving the targeted delivery functions dictated by their exosomal origin. This study demonstrates the feasibility of a mix-and-load method for rapid and efficient drug loading into exosomes, with significant potential for the treatment of neurological diseases.

Exosomes are major transport mediators of RNA, proteins, and other molecules between cells[1,2]. Recent studies have shown that exosomes can effectively penetrate multiple biological barriers, including the blood-brain barrier (BBB), which is known for its selectivity and dynamic nature in regulating the passage of substances such as nutrients, ions, and drugs[3,4]. Inspired by the biological role, there has been a surge of research on utilizing exosomes as drug carriers[2,5]. Among many, loading large drugs onto exosomes is perceived as one of the major challenges because of the resilient lipid membrane[6,7]. Conventional physical and/or chemical methods for drug loading irreversibly modulate the lipid membrane and embedded biomolecules. In addition, these methods are not compatible with loading nucleic acids and large proteins[8,9]. Given the critical role of RNA- and protein- based therapeutics highlighted during the COVID-19 pandemic, a non-destructive and universal drug-loading methodology for large therapeutic molecules

[1]Division of Bio-Medical Science &Technology, KIST School, University of Science and Technology, Seoul 02792, Republic of Korea. [2]Center for Advanced Biomolecular Recognition, Korea Institute of Science and Technology (KIST), Seoul 02792, Republic of Korea. [3]Brain Science Institute, Korea Institute of Science and Technology (KIST), Seoul 02792, Republic of Korea. [4]School of Mechanical Engineering, Yonsei University, Seoul 03722, Republic of Korea. [5]Yonsei-KIST Convergence Research Institute, Yonsei University, Seoul 03722, Republic of Korea. [6]These authors contributed equally: Gamsong Son, Jiyoung Song. ✉e-mail: hongnam.kim@kist.re.kr; cuboplex@kist.re.kr

that essentially preserves the biological functions of exosomes is of great interest.

Membrane fusion-based vesicular delivery is an emerging approach to drug loading in exosomes[10]. This non-destructive method allows for the loading of large therapeutic molecules, with drug size limitations determined primarily by the encapsulation capacity of the fusogenic carrier[11]. Recently, there have been multiple attempts to deliver drugs onto exosomes through membrane fusion with drug-encapsulating liposomes[12–14]. However, the liposome-based membrane fusion method requires multiple processing steps and/or long processing times (>12 h) due to the low fusogenicity[12,13]. Moreover, the liposome-based method requires the use of high concentrations (>50 mol%) of cationic lipids in liposomes to encapsulate anionic molecules such as mRNA[15,16]. This limitation also applies to RNA delivery into exosomes, where cationic liposomes have been commonly used[17,18]. This can significantly alter the membrane charge density of the hybrid exosomes, potentially leading to increased cellular toxicity and limited tissue penetration[19,20].

Cubosomes are highly fusogenic lipid nanoparticles, with bicontinuous cubic symmetry[21]. According to membrane elasticity theory, the lipid bilayer in cubosomes has a positive Gaussian modulus allowing for spontaneous membrane fusion[22–25]. Cubosomes are known for their versatility in encapsulation, capable of encapsulating both hydrophilic and hydrophobic molecules[26]. Notably, recent studies have demonstrated their ability to successfully encapsulate mRNA, underscoring their suitability for delivering large-sized therapeutic molecules[27]. Moreover, cubosomes serve as excellent drug reservoirs; their small water channels, where hydrogen-bonded water molecules to lipid head groups limit the degradation and conformational changes of encapsulated molecules. Considering the superior fusion characteristics and high encapsulation capacity of cubosomes, it can be a superior candidate for loading drugs into exosomes.

In this study, we report a cubosome-mediated universal and rapid drug loading method for exosomes that preserves the function of embedded biomolecules. The drug loading capability of cubosomes was demonstrated with various drugs of different sizes and physicochemical properties, including doxorubicin, immunoglobulin G, and mRNA. The functional behaviors of the resulting hybrid exosomes were assessed through permeability tests conducted in a BBB-on-a-chip model. Notably, the hybrid exosomes exhibited varying transport across the BBB and cellular uptake behaviors depending on the cubosome-exosome ratio and their cellular origin, suggesting that they retain the functional properties of the original exosomes post-fusion. We propose that our hybrid exosome platform offers innovative and modular strategies for therapeutic delivery in CNS disorders.

Results and discussion

In this work, we utilized cubosomes to load drugs into exosomes (Fig. 1a). Cubosomes are highly fusogenic lipid nanoparticles having two principal curvatures with different signs, similar to fusion pore. According to the membrane elasticity theory, this structure can spontaneously fuse with lipid membrane by lowering the free energy cost upon fusion (please refer to the method section for detail)[24]. Due to the high fusogenicity of cubosomes, we can simply mix solutions of cubosomes and exosomes to fabricate hybrid exosomes. The preservation and enhancement of biological functions of hybrid exosomes were demonstrated with an in vitro BBB permeation test (Fig. 1b). The hybrid exosomes retained the intrinsic properties of the exosomes dictated by their origin, and the cubosome-to-exosome ratio modulated the BBB permeability and absorption behavior.

Cubosome mass production

Our previous study demonstrated a microfluidic approach for cubosome fabrication[28]. However, the production rate of cubosomes was aproximately 20 times lower than that of lipid nanoparticles (LNPs), which limited their utility in translational research[28–30]. Here, we optimized flow conditions and the microfluidic mixer design for large-scale production (Fig. 2a). The lipid feeding solution and water were simultaneously injected and mixed through the microfluidic mixer. Upon mixing, solvent polarity abruptly changed, leading to lipid precipitation into droplets (Supplementary Fig. 1e). Subsequently, these droplets were annealed to induce fusion between droplets and self-assembly into cubosomes.

As the primitive cubic phase is a thermodynamic equilibrium phase for the given lipid composition, we hypothesized that larger particle sizes would favor the formation of the cubic phase over other structures (Fig. 2b). According to the reported LNP studies, it is found that an increase in lipid concentration results in larger particle size[31,32]. Similarly, increasing the total flow rate (TFR) and decreasing the flow rate ratio (FRR) increases the lipid concentration in the mixed volume. Therefore, the cubic phase is expected to be favored at higher lipid concentrations, higher TFRs, and lower FRRs[33]. To prove our hypothesis, we explored the effect of these three variables on lipid nanoparticle structure within the following ranges: lipid concentration (0.15, 0.3, 0.45 M), TFR (2, 3, 4 ml/min), and FRR (water:lipid = 1:1, 2:1, 3:1).

The particle structures prepared from 27 fabrication conditions are represented as a 3D diagram (Fig. 2c). The structure of the lipid particles was analyzed by SAXS scans (Supplementary Tables 1, 2). The red, gray, yellow, and blue symbols represent the cubic, cubic dominant (cubic + hexagonal), hexagonal dominant (cubic + hexagonal), and hexagonal phases, respectively. Immediately, one can notice that the cubic phases exist in the upper right corner of the phase space. To study the trend of the lipid nanoparticle structure according to each variable, the 2D projection graphs are shown (Fig. 2d–f). Each point in the 2D diagram represents the overlap of three data points from each plane in the 3D diagram. The circles were divided into three parts, each representing the phases observed. The area where the cubic phase appeared at least once was indicated by a red background. In the lipid concentration and FRR plane, the cubic phase was prominent at higher lipid concentration and lower FRR (Fig. 2d). In the case of TFR and lipid concentration, higher lipid concentration and TFR favored the cubic phase (Fig. 2e). Lastly, TFR and FRR plane show that the cubic phase is produced in most cases, implying that lipid concentration is the most dominant parameter for structure determination (Fig. 2f). Overall, the preference for the cubic structure increased with increasing lipid concentration and TFR and decreasing FRR as we hypothesized. Indeed, it was found that cubosomes have a bigger particle size compared to lipid nanoparticles having different structures (Supplementary Fig. 1a). The manufacturing conditions for cubosomes are fixed for the remainder of the study at 0.45 M lipid concentration, 4 ml/min TFR, and 1.5:1 FRR.

Cubosomes fabricated under these conditions had a size of approximately 120 nm and a PDI of 0.17 (Fig. 2g). The 1D and 2D SAXS scan data of cubosomes represent three characteristic Bragg peaks (Fig. 2h). These three peaks appear at positions with ratios of √2, √4, and √6, corresponding to [110], [200], and [211] reflections, respectively. The calculated lattice spacing was 154.4 Å. Additionally, SAXS analysis of dye-loaded cubosomes (Supplementary Fig. 1b) confirms that the lipid composition used in this study supports the formation of a long-range ordered bicontinuous cubic phase. The detailed structure of cubosome was studied using cryo-EM (Fig. 2i). In line with results obtained from other techniques, cubosomes have 121 ± 12 nm in size and well-ordered internal structures (Supplementary Fig. 1d).

Drug encapsulation in cubosome

Cubosome is composed of two interwoven water channels separated by a continuous lipid bilayer[33]. Therefore, it can encapsulate both hydrophilic and hydrophobic drugs. Among many drugs, large-sized biomolecules such as mRNA and proteins (>100 kDa) have garnered

https://doi.org/10.1038/s41467-025-59489-5

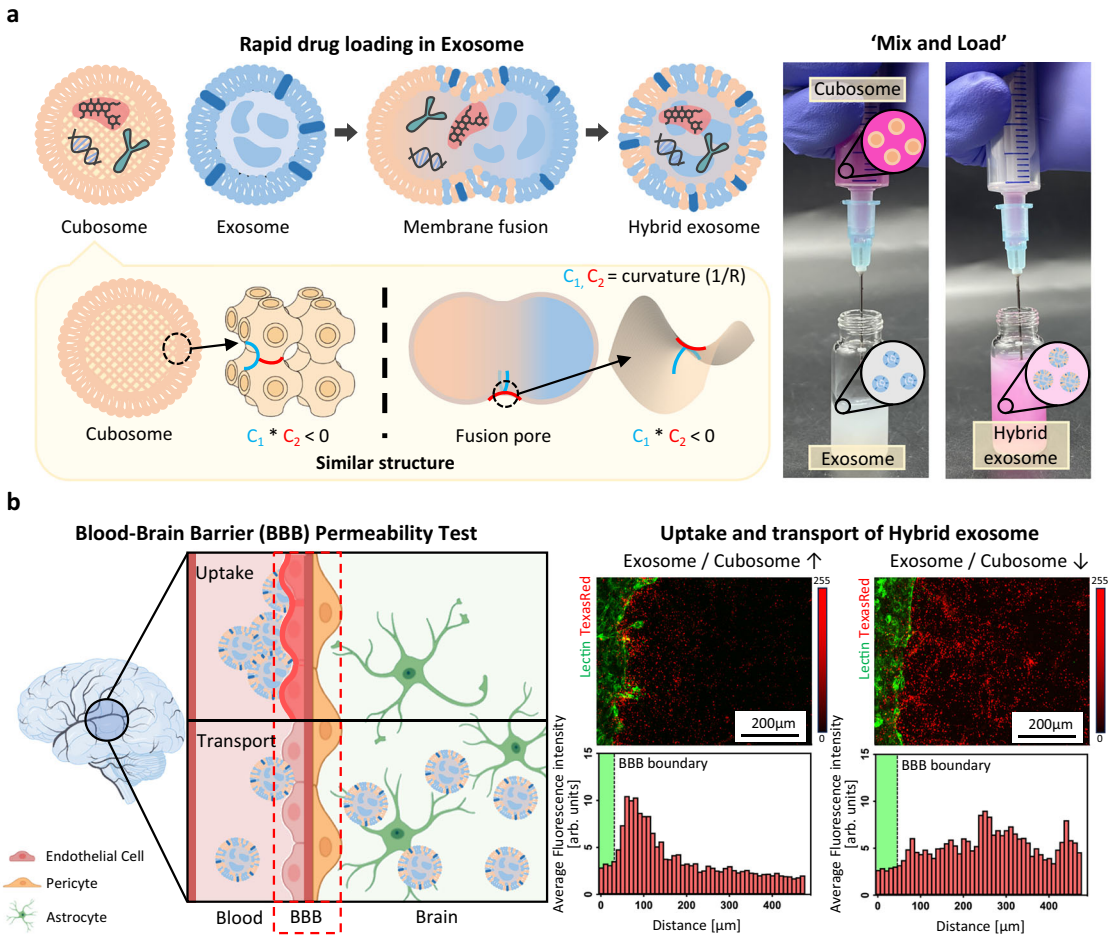

Fig. 1 | Rapid loading of large therapeutic molecules into exosomes. **a** Schematic of the membrane fusion process between fusogenic lipid nanoparticle (cubosome), and exosome for rapid and efficient drug loading into exosomes. The rapid membrane fusion allows a simple workflow, mix-and-load. **b** Blood-brain barrier permeability test of hybrid exosomes. Exosome / Cubosome ratio can modulate BBB uptake and transport. **b** Created in BioRender. Song, J. (2025) https://BioRender.com/6p849jp.

significant interest since COVID-19. To load such molecules onto exosomes, we first aimed to encapsulate large-sized therapeutic molecules in cubosomes.

To encapsulate drugs into cubosomes, we mixed the drug-feeding solution with the lipid solution using a microfluidic mixer (Fig. 3a). Upon mixing, drug-encapsulating droplets were generated and subsequently fused to form cubosomes during the annealing process. We then analyzed the amounts of drugs loaded into the cubosomes. For doxorubicin and IgG, loading efficiency was over 85% (Fig. 3b). Surprisingly, long mRNA (1 kb) showed a loading efficiency reaching 98% based on RiboGreen assay. In fact, this result can be expected, considering that similar manufacturing methods used in LNPs have also shown high encapsulation efficiency for mRNA[34]. The encapsulation of mRNA in cubosome was further validated by fluorescence microscopy. Cubosomes were stained red with Texas Red dye (Fig. 3c), and mRNA was labeled green with FAM dye (Fig. 3d). When two images were overlapped, the yellow particles were observed, indicating that mRNA is colocalized within the cubosomes (Fig. 3e). Green particles were rarely observed, suggesting that most of the mRNA is loaded into the cubosomes as observed in the loading efficiency test.

For effective drug loading into exosomes in the later stage, it is important for mRNA-cubosomes to maintain fusogenic structure. The size of mRNA-cubosomes was 101.6 nm, about 20 nm smaller than drug-free cubosomes (Fig. 3f). The smaller size is attributed to the Coulombic interaction between mRNA and the cationic lipid. In the 1D SAXS plot, three characteristic Bragg peaks are observed at the same q values as in the cubosome-only samples, indicating a well-ordered primitive cubic structure (Fig. 3g). As expected, the zeta potential of cubosomes encapsulated with negatively charged mRNA decreased (Supplementary Fig. 2e). Interestingly, a distinct peak around 0.12 $Å^{-1}$ appeared, which was not observed in cubosome-only samples. According to foundational work by the Safinya group, this peak can be interpreted as the folding structure of the mRNA[35,36]. Based on the position and width of the mRNA peak, we can infer that mRNA forms units spaced 5.1 nm apart, with approximately 3.7 repeating units. The Cryo-EM image of the mRNA-cubosome further supports the presence of a highly ordered internal structure, as indicated by the SAXS study (Fig. 3h, Supplementary Fig. 2a). Cubosomes loaded with IgG and Dox retained a well-ordered cubic structure, demonstrating their versatility for loading various drug types (Supplementary Fig. 3a,b).

Cubosome as an excellent drug reservoir

In addition to their high encapsulation efficiency, cubosomes demonstrate an excellent capacity to protect encapsulated molecules from environmental degradation. This is particularly crucial for maintaining the stability of sensitive agents such as mRNA. Considering the mix-and-load scenario, room temperature storage is beneficial for the effective distribution of exosome therapies.

We studied the structural stability of mRNA-cubosomes by storing the mRNA-cubosome solution at room temperature for three weeks. The changes in the cubic structure of lipids and the folding structure of mRNA were monitored using SAXS (Fig. 3i). Typically, oxidation of

https://doi.org/10.1038/s41467-025-59489-5

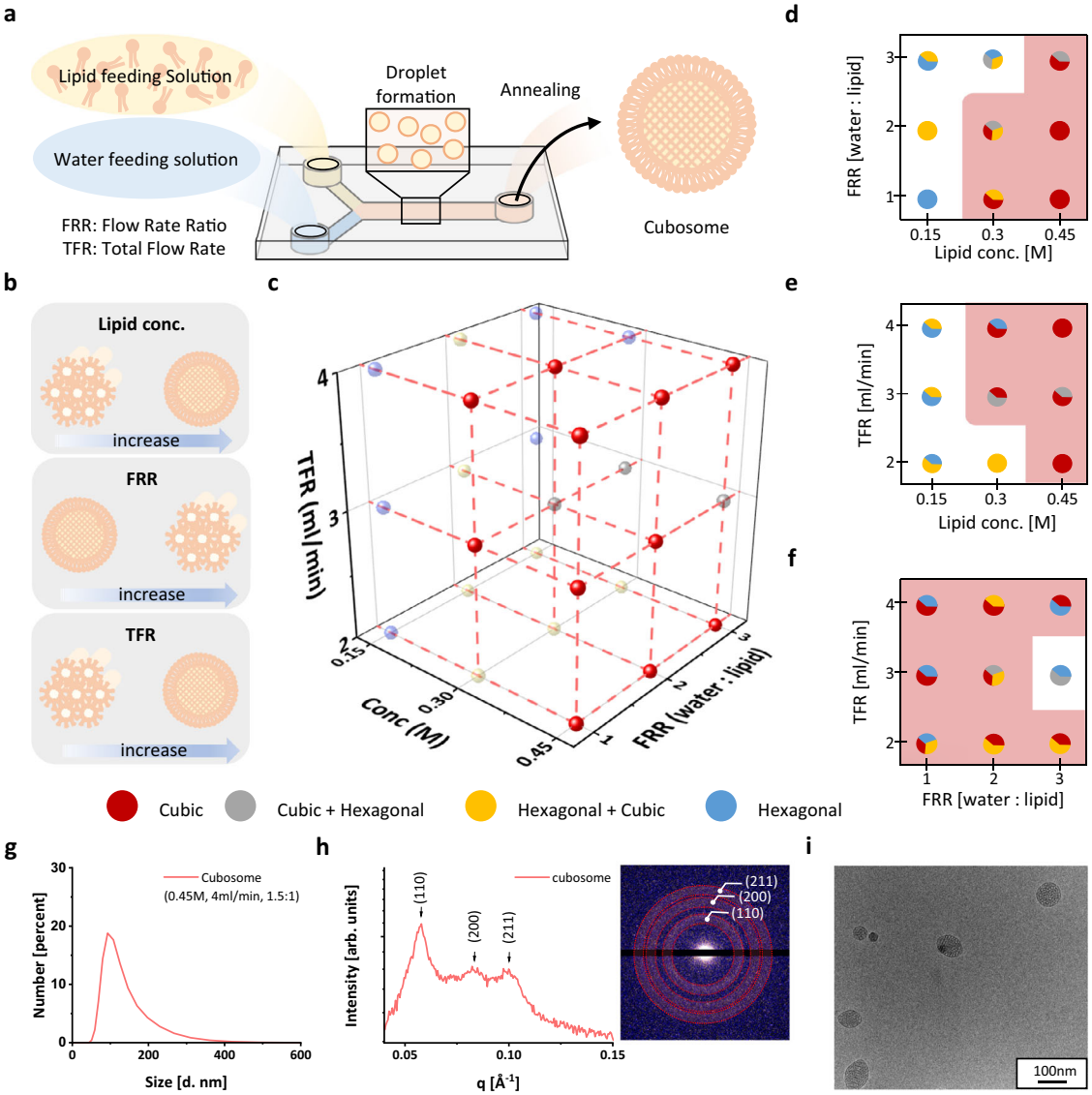

Fig. 2 | Optimize cubosome fabrication for mass production. a Schematic of cubosome fabrication using microfluidic mixer. When the solvent polarity changed abruptly upon mixing of two solutions, lipids precipitate into droplets. Afterwards, annealing of droplets induces the self-assembly into cubosomes. Lipid concentration (0.15, 0.3, 0.45 M), Flow rate ratio (FRR; lipid:water = 1:1, 1:2, 1:3), and total flow rate (TFR; 2, 3, 4 ml/min) were controlled independently. **b** Preferred lipid phases according to lipid concentration, FRR, and TFR. **c** 3D phase diagram representing the phases of 27 samples at varied lipid concentrations, FRR, and TFR. Red circle indicates a cubic phase. Gray circle represents coexistence of cubic and hexagonal phases, but cubic phase is dominant. Blue circle, on the other hand, represent the hexagonal phase dominant. Pure hexagonal phases are marked with green circles. **d**–**f** 2D projection diagrams of concentration-FRR, concentration-TFR, and FRR-TFR plane. Each circle is divided into three parts to indicate the overlapping color results of three replicate samples. Areas where the cubic phase appeared at least once are marked with a red background. **g** DLS results under the final condition (0.45 M, lipid:water = 1:1.5, 4 ml/min). **h** SAXS results and 2D-SAXS image under the final conditions revealing a well-ordered primitive cubic phase. **i** Cryo-TEM image under the final conditions.

lipid head groups can lead to structural changes and mRNA can easily degrade under these conditions. However, the mRNA-cubosomes maintained a unit cell size of 15.37 ± 0.10 nm and mRNA repeating units (domain size/unit spacing(d_{mRNA})) of 3.58 ± 0.14 throughout the three weeks (Fig. 3j). The photographic images of fresh and three-week-old samples show a consistent milky color, demonstrating the colloidal stability of mRNA-cubosomes (Fig. 3k). Therefore, cubosomes offer a promising solution for the effective storage and distribution of sensitive drugs such as mRNA, thereby enhancing the viability of exosome therapies.

Kinetics of membrane fusion

Next, we evaluate the kinetics of fusion between cubosomes and exosomes via Fluorescence Resonance Energy Transfer (FRET) analysis. Cubosomes were prepared with FRET pairs (0.5 mol% of NBD-PE and Liss Rhod-PE each) (Fig. 4a, Supplementary Fig. 1b). When these two dyes in the cubosome are close enough and excited by 460 nm light, emission occurs at 590 nm through energy transfer from NBD to Liss Rhod. When membrane fusion between cubosome and exosome happens, the distance between NBD and Liss Rhod would increase, leading to a decrease in the fluorescence intensity of Liss Rhod. The changes in Liss Rhod fluorescence intensity over 10 min were monitored. As the cubosome-to-exosome ratio decreased, the Liss Rhod fluorescence intensity decreased more rapidly, and the fusion rate saturated at a cubosome: exosome ratio of 1:5 (Supplementary Fig. 4a). Therefore, to show the overall trend, we finally selected the ratios of 1:1 and 1:10, which represent slow and fast fusion kinetics, respectively. Regardless of the cubosome to exosome ratio, a rapid decrease in Liss

https://doi.org/10.1038/s41467-025-59489-5

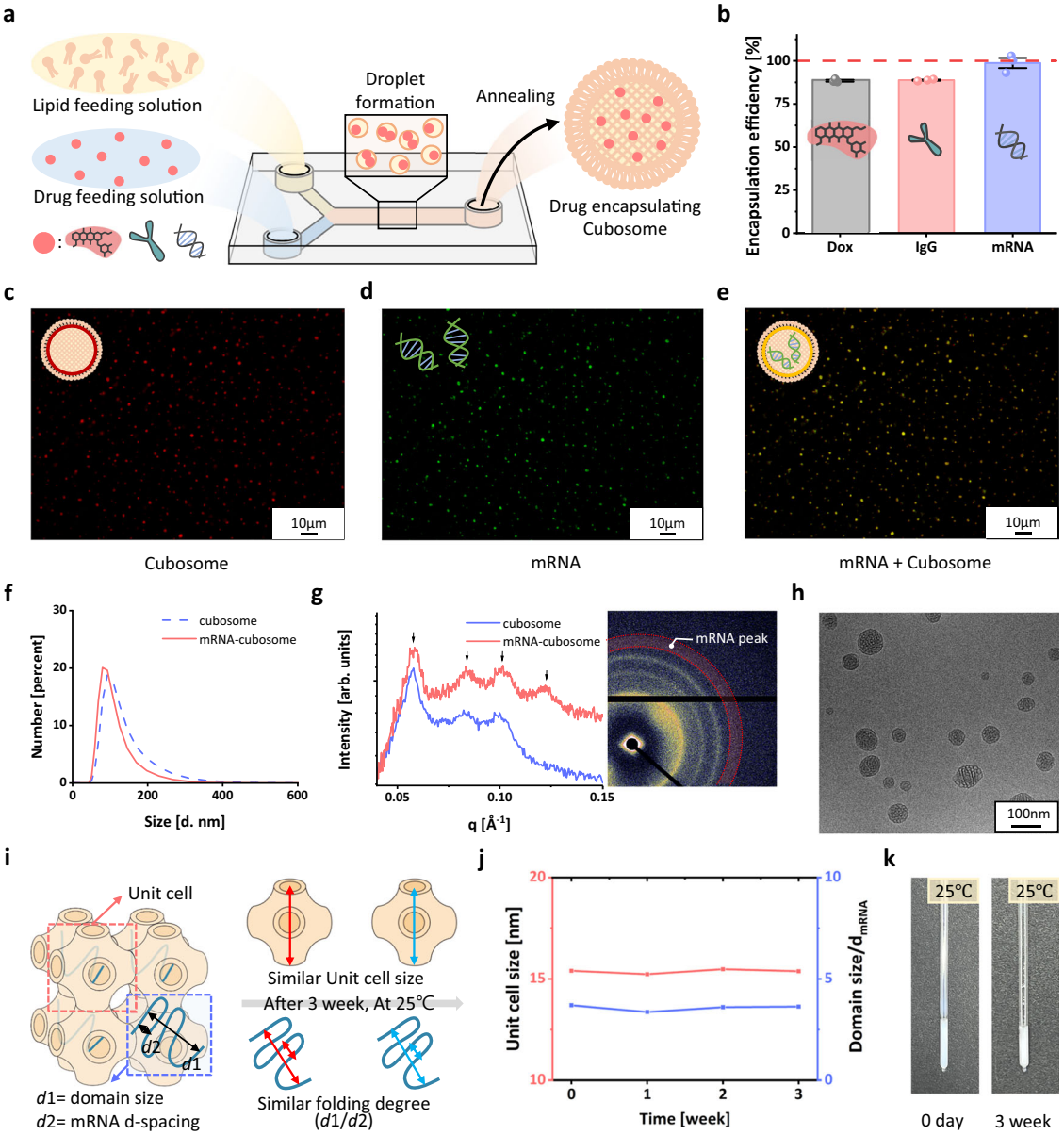

Fig. 3 | Bottom-up approach for drug encapsulation in cubosome. a Bottom-up strategy of drug encapsulation in cubosome using a microfluidic mixer. Drug-encapsulating droplets are fused to form a cubosome during the annealing process. **b** Encapsulation efficiency in cubosome for three different types of drugs; doxorubicin, immunoglobulin G, and mRNA. Data are presented as mean ± SE, $n = 3$. **c**–**e** Fluorescence optical microscope images showing mRNA loaded cubosomes. Cubosomes were labeled by Texas Red **c**, mRNAs were labeled by FAM **d**. Merged images of cubosome and mRNA **e** show yellow particles indicating co-localization of mRNA and cubosome. **f** DLS results for cubosome and mRNA-cubosome, showing the decrease of particle size upon mRNA encapsulation. **g** 1D and 2D SAXS scan results of cubosome and mRNA-cubosome samples, showing an mRNA specific peak that is only observed in mRNA-cubosome sample. **h** Cryo-TEM image of mRNA-cubosome showing the uniform size distribution and well-ordered internal structure as seen in SAXS and DLS studies. **i** Illustration of cubosome and mRNA conformation (folding degree is defined as domain size / mRNA d-spacing) in cubosome. **j** Unit cell size of cubosome and mRNA folding degree were maintained even after storing for 3 weeks at room temperature. **k** Optical images of mRNA-cubosome solution after 0 day and 3 weeks at room temperature.

Rhod fluorescence intensity was observed when the buffer was deionized water (Fig. 4b,c and Supplementary Fig. 4b–e). To investigate the impact of electrostatic force on the fusion between cubosomes and exosomes, the same experiments were also conducted but in PBS buffer condition. Interestingly, fusion in PBS exhibited considerably slower kinetics and the effect of cubosome to exosome ratio was more prominent in PBS buffer condition.

Although lipid mixing is a generally accepted indicator of the membrane fusion process, it can only provide information about lipid mixing between cubosomes and exosomes. As our goal is to maintain the vesicle structure after the fusion event, the completion of fusion needs to be monitored. Therefore, we utilized Small Angle X-ray Scattering (SAXS) to estimate the fusion structures. After mixing cubosomes and exosomes at a number ratio of 1:10 in deionized water, in situ SAXS scans show the time-dependent scattering changes at 10-s intervals for 10 min (Fig. 4d). Three Bragg peaks at the initial time point indicate the presence of well-ordered cubosomes in the sample. Over time, the intensities of the Bragg peaks continuously decrease and disappear. When we plotted the intensity of the first Bragg peak over time at 60-s intervals after background subtraction, a trend similar to that observed in the FRET study was found (Fig. 4e,f). Cubic structure disappears much faster in deionized water, while cubic structure

https://doi.org/10.1038/s41467-025-59489-5

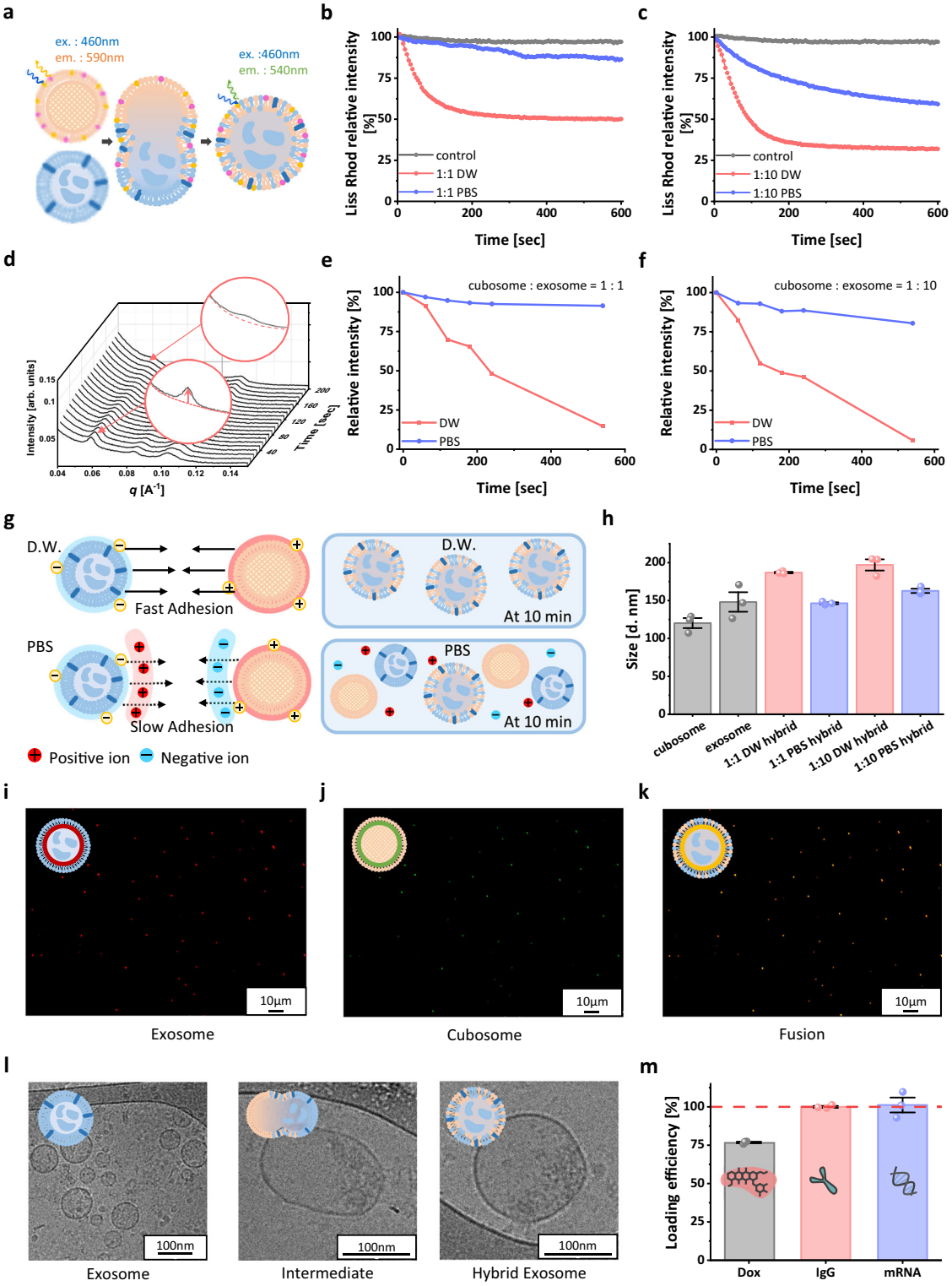

remains when fusion happens in PBS buffer. When cubosome to exosome number ratio was 1:10 and mixed in PBS buffer, however, the intensity of the Bragg peak was rather preserved over 10 min. In other words, even though lipid mixing happens rapidly in this condition, it forms intermediate structures, for example, cubosome-attached exosomes (bleb structure).

The schematic illustration of membrane fusion from a structural perspective is summarized in Fig. 4g. The ions in PBS screen the electrostatic interactions between positively charged cubosomes and negatively charged exosomes, slowing down the fusion process[37,38]. Indeed, Debye lengths were calculated as 203 nm in deionized water and 35.8 nm in PBS, supporting the dramatic difference in fusion kinetics between the two different buffers. Another variable, the cubosome to exosome number ratio, also affects the fusion kinetics. In the case of 1:10 ratio, the Liss Rhod fluorescence intensity decreased by 57% after 10 min of mixing, but in the case of 1:1 the rate decreased only by 12% in PBS. We can understand the fusion behavior at different particle concentrations using Collision Theory, a model that explains reaction rates. In the context of fusion events, the fusion reaction is governed by the collision between particles. According to the theory,

Fig. 4 | Membrane fusion between cubosome and exosome. a Scheme of describing the Fluorescence Resonance Energy Transfer (FRET) experiment for understanding fusion kinetics at different exosome: cubosome ratio and buffer. As fusion progresses, the energy transfer between FRET pair is decreased. The fluorescence intensity decrease of acceptor, Liss Rhod dye, was used as a lipid mixing indicator. Cubosomes were used as a control for comparison before fusion occurred. **b** Changes in fluorescent intensity of Liss Rhod intensity in Deionized water (D.W.) and PBS when the exosome: cubosome number ratio is 1:1. **c** Changes in Liss Rhod intensity in D.W. and PBS when the exosome: cubosome number ratio is 10:1. **d** SAXS scan results for solution of cubosome and exosome mixture. Under D.W. conditions, measurements were taken every 10 s for 10 min when the exosome: cubosome concentration ratio was 10:1. As fusion progresses, the intensity of the first Bragg peak indicating cubic phase is decreased. **e** Changes in the first peak of the cubic phase in D.W. and PBS when the exosome: cubosome concentration number ratio is 1:1. **f** Changes in the first peak of the cubic phase in D.W. and PBS when the exosome: cubosome concentration number ratio is 10:1. **g** Scheme showing the difference in the membrane fusion kinetics in D.W. and PBS due to charge screening. **h** DLS results in D.W. and PBS when the exosome: cubosome concentration ratio is 1:1 and 10:1. Data are presented as mean ± SE, $n = 3$. **i** Fluorescence image of hybrid exosome showing only the exosome labeled by DiI. **j** Fluorescence image of hybrid exosome showing only the cubosome labeled by NBD-PE. **k** Fluorescence image of hybrid exosome. Exosome and cubosome overlap and yellow signal observed, supporting a completion of membrane fusion. **l** Cryo-TEM image of the fusion process between exosome and cubosome. **m** Loading efficiency of doxorubicin, immunoglobulin G, and mRNA into exosomes. Data are presented as mean ± SE, $n = 3$.

the collision frequency is proportional to the concentrations of the reacting species, as described by the equation:

$$Z_{AB} = N_A N_B \sigma_{AB} \sqrt{\frac{\pi\mu}{8kT}} \quad (1)$$

Where Z_{AB}: Collision Frequency, N_A,N_B: Number of Particle A and B, σ_{AB}: Collision Cross-Section, μ: Reduced Mass, k: Boltzmann Constant, T: Temperature[39]. As the concentration of reactant particles increases, the number of collisions rises, thereby increasing the likelihood of a reaction. Thus, an increase in the concentration of exosomes leads to more frequent collisions with cubosomes, promoting faster fusion.

The fusion reaction between cubosomes and exosomes in D.W. was mostly completed within 10 min, indicating the fast fusion kinetics. The underlying principle of such kinetics can be understood using membrane elasticity theory by Helfrich[24]. According to the theory, the free energy of a membrane per unit area can be described as follows:

$$F/A = k/2(C - C_0)^2 + \bar{\kappa}K \quad (2)$$

Where C and C_0 represent curvature and equilibrium curvature of a membrane, $\bar{\kappa}$ and K are Gaussian moduli and Gaussian curvature, respectively. The free energy change during membrane fusion is about $-4\pi\bar{\kappa}$ (Please refer method section for details). In the case of cubosomes, $\bar{\kappa}$ is positive so the fusion is spontaneous while this is not the case for liposomes.

Characterization of fusion structures

After confirming the fast fusion event between cubosome and exosome, we studied the size change of the system as fast kinetics may indicate large aggregates. After 10 min of mixing cubosome and exosome solutions, the size increased as we expected in all systems (Fig. 4h). As the number concentration of exosomes increased during fusion, the particle size also increased, suggesting that the higher concentration facilitated the interaction between the two particles. However, the particle diameter stayed below 200 nm in all fusion conditions, indicating that fused lipid nanoparticles have slower fusion kinetics over time. As observed in the lipid mixing experiments, electrostatic interactions are the major driving force for fusion. When membrane fusion happens, the effective membrane charge density decreases, thereby limiting the chance of colliding with another lipid nanoparticle[40,41]. The smaller size of lipid nanoparticles fused in PBS buffer at a cubosome-to-exosome number ratio of 1:10 (163 nm) compared to the sample in deionized water (197 nm) further concretes this hypothesis. When we increased the incubation time to several hours, however, the particle size increased significantly in the case of excess exosomes incubated with cubosomes in deionized water (Supplementary Fig. 5d,e).

To evaluate the overall degree of fusion, we utilized fluorescence microscopy. Cubosomes were labeled with the green fluorescent dye, NBD-PE, and exosomes were labeled with the red fluorescent dye, DiI. Two solutions of cubosomes and exosomes were then mixed at a 1:10 ratio in deionized water and imaged after 10 min (Fig. 4i,j). In the merged fluorescence image, most particles appeared yellow, indicating colocalization of cubosomes and exosomes (Fig. 4k). Additionally, the absence of green fluorescence suggests that all of the cubosomes fused with exosomes within 10 min.

To understand the detailed membrane fusion structures, we conducted Cryo-TEM studies (Fig. 4l). Exosomes were characterized by an electron-dense core (from exosomal proteins and nucleic acids) with heterogeneous size distribution. When exosomes and cubosomes are in contact, they rapidly exchange lipids and form an active fusion pore. In the middle of the cryo-EM image, one can see the intermediate fusion structure with electron-dense materials appearing to be biased on one side suggesting membrane fusion between cubosomes and exosomes. Subsequently, the fully fused hybrid exosome appeared where the proteins of the exosome dispersed throughout, indicating complete fusion.

Finally, we studied whether the drugs encapsulated in the cubosome can be transferred to the inside of the exosome. Each of the three cubosome solutions encapsulating different drugs was mixed with exosomes for 10 min. To minimize the number of unfused cubosomes, the number ratio of cubosomes to exosomes was set at 1:10. The drug loading efficiency was then measured (Fig. 4m). Doxorubicin showed a relatively low delivery efficiency of approximately 77%. This is because, similar to the previous cubosome loading, doxorubicin has higher membrane permeability compared to other drugs, allowing it to transport freely across the membrane. Remarkably, most of the IgG and mRNA were transferred to the exosome without detectable loss.

Transport of hybrid exosomes in BBB model

To study whether hybrid exosomes retain the unique transport capability of exosomes, we evaluated the transport of hybrid exosomes across the in vitro 3D BBB model. For this purpose, we utilized microphysiological system-based BBB models which offer multiple benefits, including visualization of drug carrier transport, discrimination of uptake and transport, and cell type-specific uptake.

To generate the in vitro 3D BBB model, a microfluidic device consisting of three-phase guide channels (microstructures that guide the liquid flow in microchannels) was utilized (Fig. 5a)[42]. To recapitulate human brain BBB physiology, a hydrogel suspension mixed with human astrocytes (HAs) and human brain vascular pericytes (HBVPs) was introduced into the central channel of the device and allowed to gelate. The following day, human brain microvascular endothelial cells (HBMECs) were evenly seeded on the hydrogel wall, as well as on the bottom and top of the side channels. The tri-cultured system was then incubated for fourdays to facilitate maturation of the endothelial barrier. The microfluidic platform is optimized for high-throughput studies, as it contains 28 individual wells per device and requires only 1 μL of hydrogel per well, significantly reducing reagent consumption

https://doi.org/10.1038/s41467-025-59489-5

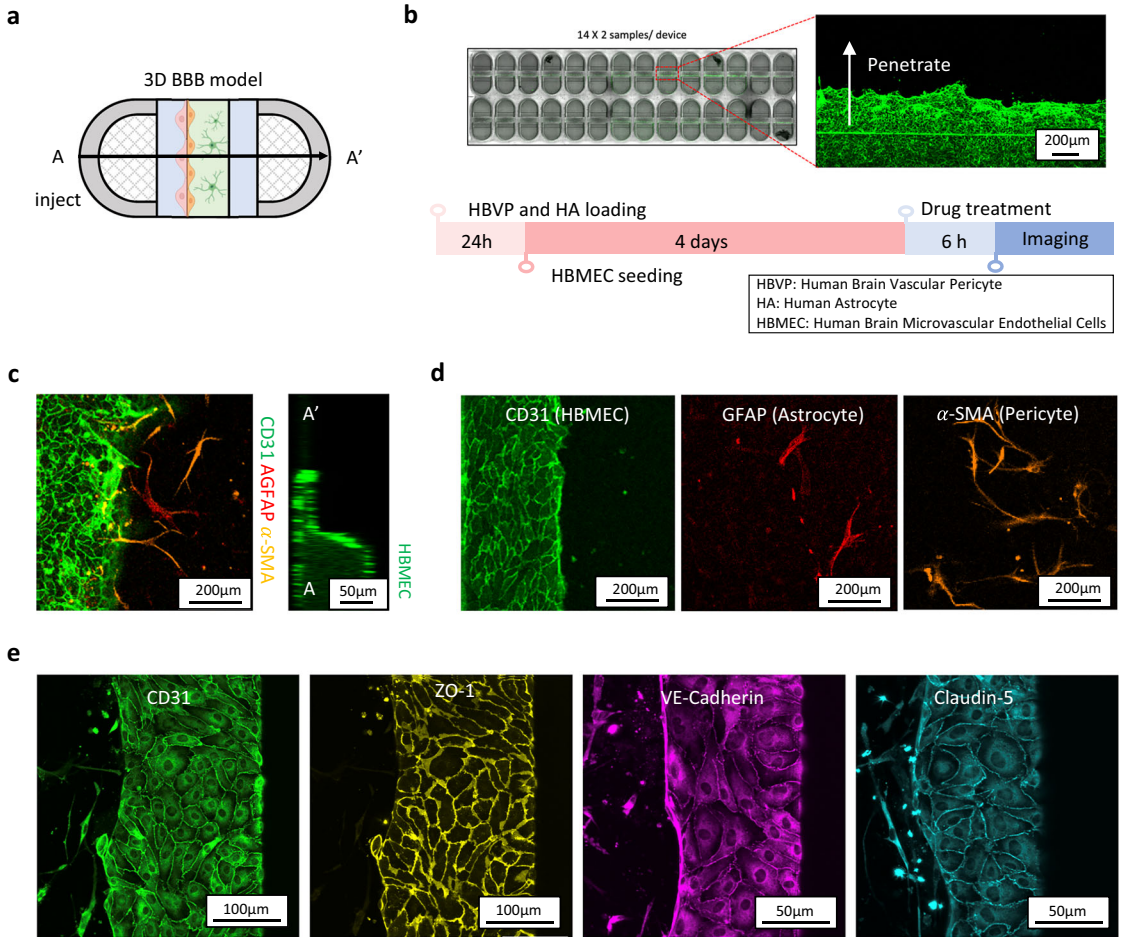

Fig. 5 | Reconstruction of the in vitro BBB model. a A scheme showing a 3D BBB model with three-phase guide channels. **b** Entire image of the microfluidic device and the process of creating an in vitro 3D BBB model and permeability test. **c** Confocal image showing cells cultured in the 3D BBB model. **d** In the 3D BBB model, human brain microvascular endothelial cells (HBMEC), human astrocytes (HA), and human brain vesicular pericytes (HBVP) are labeled with CD31(green), GFAP(red), and αSMA(orange), respectively. **e** Visualization of tight junction proteins in the endothelial cell layer, confirming the integrity and maturity of the endothelial barrier: CD31 (green), ZO-1 (yellow), VE-cadherin (purple), and Claudin-5 (cyan). **a** Created in BioRender. Song, J. (2025) https://BioRender.com/o9v2cps.

while enabling efficient evaluation of drug permeability across the BBB (Fig. 5b). To validate the formation and integrity of the BBB model, we performed immunofluorescence staining using specific cellular markers (Fig. 5c). Endothelial cells (HBMECs) were stained with CD31, astrocytes with GFAP, and pericytes with αSMA. The results showed that endothelial cells formed a continuous monolayer barrier that closely interacted with the astrocytes and pericytes along the hydrogel interface (Fig. 5d). Additionally, the presence of key tight junction proteins, including ZO-1, VE-cadherin, and Claudin-5, confirmed the integrity of the endothelial barrier and its maturation after a four-day incubation period (Fig. 5e). Astrocytes and pericytes were observed lining the hydrogel surface, forming a structure that mimics the in vivo BBB. Collectively, these results demonstrate that the developed in vitro BBB model successfully recapitulates the essential cellular architecture, tight junction integrity, and functional properties of the native BBB, making it a powerful platform for drug permeability studies.

We evaluated the transport of hybrid exosomes across an in vitro 3D BBB model. Red fluorescent dyes (DiI and Texas Red for exosome and hybrid exosome, respectively) conjugated carriers were used to visualize the transport of the carriers. Additionally, green fluorescent dye-conjugated lectins, which specifically bind to glycoproteins in endothelial cells, were used to visualize the boundary of the endothelial barrier. The fluorescently labeled carriers were added to the triculture medium and introduced into the microfluidic reservoir, which is connected to the channel where endothelial cells were being cultured. The uptake and transport of the carriers across the endothelial barrier were then monitored using confocal microscopy.

The HBMEC-derived exosomes (HBMEC-exosome alone) were preferentially uptaken by brain endothelial cells, exhibiting the highest fluorescence intensity at the BBB boundary (Fig. 6a). In the case of hybrid exosomes prepared by fusing HBMEC-exosomes with cubosomes, an enhanced BBB transport was observed compared to the HBMEC exosomes alone (Fig. 6b). Additionally, as the ratio of HBMEC exosomes decreased, the fluorescence intensity near the BBB boundary also decreased (Fig. 6c), suggesting increased transport or decreased HBMEC content-EC interaction. These results suggest that (i) the content from cubosome facilitates the transport of carriers, and (ii) the content from HBMEC-exosomes increases the uptake or interaction of carriers in the HBMEC wall. These findings also imply that the modular approach to controlling the transport-uptake ratio of target drugs is feasible by modulating the exosome-to-cubosome ratio.

One important merit of exosomes is that they have specificity based on their cellular origin. Therefore, we investigated how exosomes from different sources influence the transport of hybrid exosomes across the BBB. We prepared HA-derived exosomes and fused them with cubosomes at a 1:1 ratio (Fig. 6d). To demonstrate the difference in uptake behaviors, the carriers were identically perfused into

https://doi.org/10.1038/s41467-025-59489-5

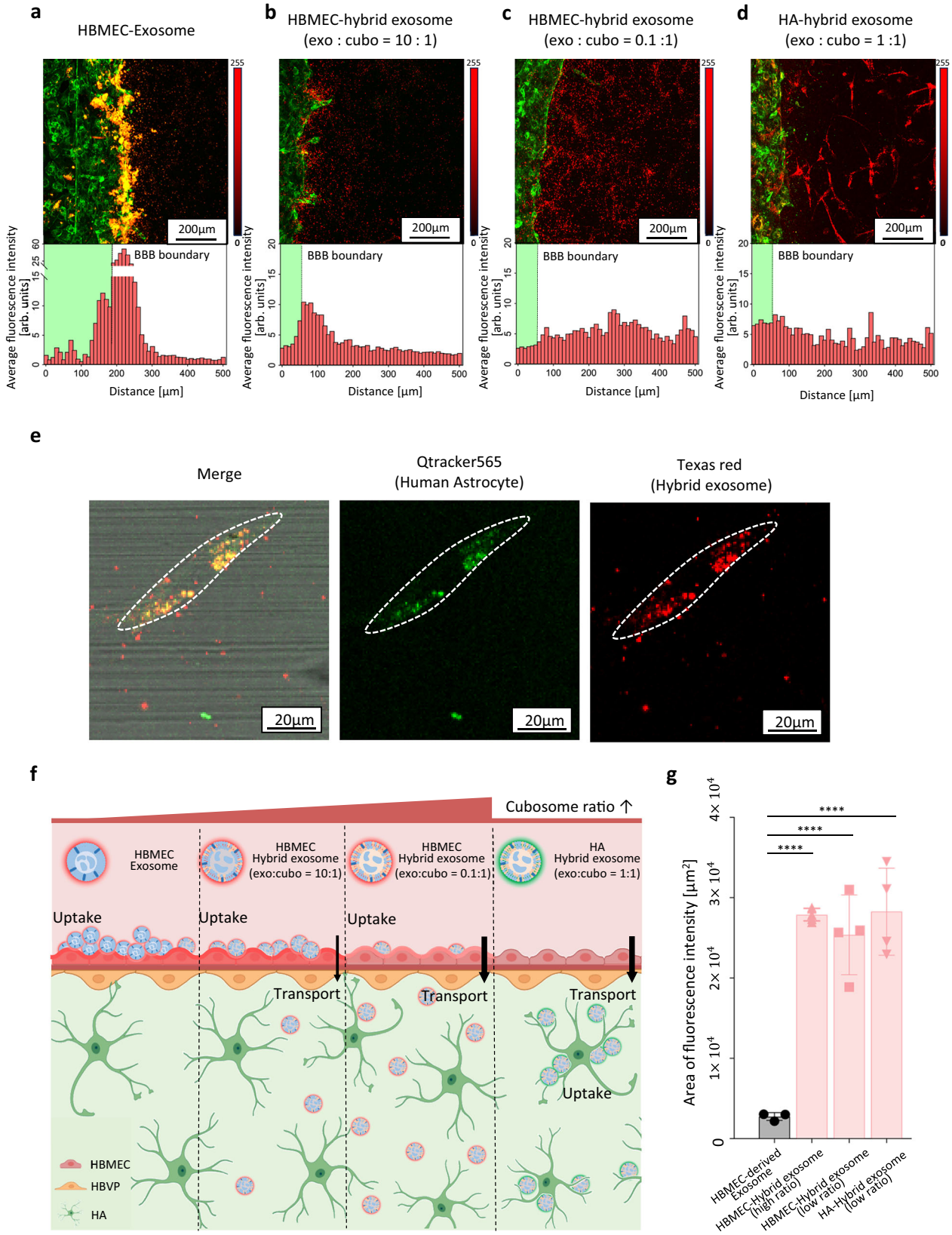

the endothelium channel and their transport was observed, focusing particularly on astrocytes within the 3D hydrogel. Interestingly, unlike HBMEC-hybrid exosomes, HA-hybrid exosomes were predominantly taken up by astrocytes within the 3D hydrogel rather than by endothelial cells. To further validate the involvement of human astrocytes (HAs), we pre-labeled astrocytes with Qtracker 565 (green), a stable long-term cell tracker, before seeding them into the microfluidic device. HA-hybrid exosomes were tagged with Texas Red (red) and perfused into the system. The confocal images demonstrated the successful crossing of the BBB by hybrid exosome and their subsequent uptake by astrocytes, as evidenced by the clear co-localization of the green (astrocyte) and red (hybrid cubosome) signals in the

Fig. 6 | Uptake and transport behavior in 3D BBB model. a–d Confocal image showing the BBB permeability results for each particle. The bar graphs illustrate the fluorescence intensity at various positions in the 3D BBB model. Endothelial cells are labeled with Lectin (green), and HBMEC-exosomes are labeled with DiI (red). HBMEC-hybrid exosomes and HA-hybrid exosomes are labeled with TexasRed (red). **e** Confocal images demonstrating the uptake of hybrid exosomes by human astrocytes labeled with Qtracker 565 (green). Texas Red-labeled hybrid exosomes (red) colocalize with astrocytes, confirming effective delivery across the BBB. Scale bars: 20 μm. **f** A scheme showing the BBB uptake and transport behavior of each particle. **g** Area of fluorescence intensity below the BBB boundary. Data are presented as mean values with SD and $n = 3–4$. Statistical significance: $^{****}p < 0.0001$. Statistical significance was determined using an ordinary one-way ANOVA followed by Tukey's multiple comparisons test. **f** Created in BioRender. Song, J. (2025) https://BioRender.com/sw5wxrk.

merged image (Fig. 6e). These results clearly indicate that the origin of exosomes influences the fate of cellular uptake after BBB penetration by hybrid exosomes.

In summary, our findings demonstrate that (i) the presence of cubosomes in hybrid exosomes enhances transport across the BBB, (ii) the cubosome-to-exosome ratio regulates the balance between transport and uptake, and (iii) the origin of the exosomes influences target of uptake through homing effects (Fig. 6f). These conclusions are clearly supported by the integrated fluorescence intensity observed outside the BBB barrier (Fig. 6g).

Transport of drug-loaded hybrid exosomes across the BBB

To evaluate the permeability of various bioactive cargoes, including doxorubicin, immunoglobulin G (IgG), and mRNA, we conducted a permeability assay using both cubosomes and hybrid exosomes in the in vitro BBB model (Fig. 7a). The results revealed that while doxorubicin showed no significant difference in permeability between cubosomes and hybrid exosomes, the transport of IgG and mRNA was significantly enhanced when delivered via hybrid exosomes. Quantitative analysis further confirmed this result, demonstrating that the permeability of IgG and mRNA increased approximately 2-fold compared to delivery with cubosomes alone (Fig. 7b). These findings indicate that hybrid exosomes exhibit superior efficiency in facilitating the transport of larger and more structurally complex molecules, such as proteins and nucleic acids, across the endothelial barrier.

To confirm that the bioactive cargo remains encapsulated and intact during transport, we tracked Texas Red-labeled hybrid exosomes (red) carrying mRNA (yellow) across the BBB model. Confocal imaging clearly showed co-localization of the red (hybrid exosome carrier) and yellow (mRNA cargo) signals beyond the endothelial barrier (Fig. 7c). This result validates that the hybrid exosomes successfully encapsulate mRNA and effectively deliver it across the BBB without significant dissociation of the cargo. Overall, these results highlight the potential of hybrid exosomes as a robust and efficient platform for the delivery of complex therapeutic molecules, particularly proteins and nucleic acids, across the BBB.

In this study, we introduced an approach for the efficient loading of large therapeutic molecules into exosomes using a simple mix-and-load method. The microfluidic method for cubosome fabrication allows the successful encapsulation of various types of drugs, including 1 kb mRNA, with minimal cationic lipid content. Our results demonstrate that cubosomes can protect encapsulated drugs such as mRNA at room temperature for up to three weeks. Remarkably, these cubosomes retained their fusogenic properties, enabling complete membrane fusion with exosomes within 10 min, thereby realizing the 'mix-and-load' method.

The BBB permeability test of hybrid exosomes demonstrates the potential in transendothelial drug delivery across the blood-brain barrier (BBB). Given the challenges associated with treating neurological disorders such as Alzheimer's disease, efficient transport of therapeutic agents across the BBB is crucial[43]. The ability to tune drug uptake and transport by adjusting the cubosome-to-exosome ratio and/or exosomal origin presents a promising avenue for developing targeted drug delivery systems.

Methods

materials

Glycerol monooleate; GMO was purchased from Nu Chek Prep(USA). 18: 1 1,2-dioleoyl-sn-glycero-3-phosphoethanolamine-N-[methoxy(polyethylene glycol)-2000] (ammonium salt); DOPE-PEG_{2000}, 18: 1 1,2-dioleoyl-3-trimethylammonium-propane; DOTAP, 1,2-dipalmitoyl-sn-glycero-3-phosphoethanolamine-N-(7-nitro-2-1,3-benzoxadiazol-4-yl) (ammonium salt); NBD-PE, 1,2-dioleoyl-sn-glycero-3-phosphoethanolamine-N-(lissamine rhodamine B sulfonyl) (ammonium salt); Liss Rhod-PE were purchased from Avanti Polar Lipids. Texas Red-DHPE, DiI cell-Labeling Solution; DiI, Human IgG total ELISA Kit, Quant-iT™ RiboGreen™ RNA Assay Kit were bought from Invitrogen. ExoQuick® kit was purchased from System Biosciences(USA). CleanCap® EGFP mRNA (5moU) (L-7201) was customized from TriLink. Doxorubicin hydrochloride; DOX, IgG from huma n serum; IgG were purchased from Sigma-Aldrich. mRNA primer (seq. [FAM] TGG GGG TGT TCT GCT GGT AGT GG) and (seq. [Cy5] TGG GGG TGT TCT GCT GGT AGT GG) was designed from BIONEER and COSMO. Phosphate-buffered saline (PBS) were purchased from Welgene and lysis buffer was purchased from Bionote, Inc (Korea). Microfluidic channel was purchased from Enparticle. Inc (Korea)

Cubosome formulation

Cubosome was manufactured using a microfluidic system. The lipid film was prepared according to each concentration (0.15, 0.3, 0.45 M) at a ratio of GMO, DOTAP, and PEG of 95:4:1 mol%. Thereafter, ethanol was added to the lipid film and then vortexed. In the water phase, each volume (500, 1000, 1500 ul) was prepared according to the ratio of FRR. The prepared water phase and lipid phase were mixed by a chaotic microfluidic mixer at 2, 3, 4 ml/min TFR. Thereafter, for the lipid emulsions were annealed by a rotary evaporation at P = 75 mbar and T = 57 °C until the final concentration reached (typically, 8–10 min). The cubosome was analyzed through DLS, SAXS, and Cryo-TEM.

Encapsulation efficiency of drugs in cubosome

The mRNA (60 μg) was dissolved in RNase-free water along with a primer labeled with FAM (60 μmol), and then dialyzed for overnight to remove free primers. Thereafter, 750 ul of mRNA solution was mixed with the lipid phase containing 0.5 mol% Texas red to form a cubosome. To confirm the loading of mRNA into the cubosomes, fluorescence microscopy was employed. Loading efficiency was calculated by separating free-mRNA through an dialysis bag (300 kDa) and then quantifying free-mRNA using a Ribogreen kit, as follows:

$$LE(\%) = \frac{intensity\ of\ cubosome\ solution\ after\ dialysis}{intensity\ of\ cubosome\ solution\ before\ dialysis} \quad (3)$$

Additional analysis was conducted using SAXS and Cryo-TEM.

Doxorubicin (Dox), Immunoglobulin G (IgG) were prepared in D.W. at concentrations of 0.5 mg and 0.51 mg, respectively. Then mixed with lipid phase as the same method. After that, through an dialysis bag (100 kDa) dialysis was performed overnight to remove free-drug. Dox and IgG calculated Loading efficiency through changes

https://doi.org/10.1038/s41467-025-59489-5

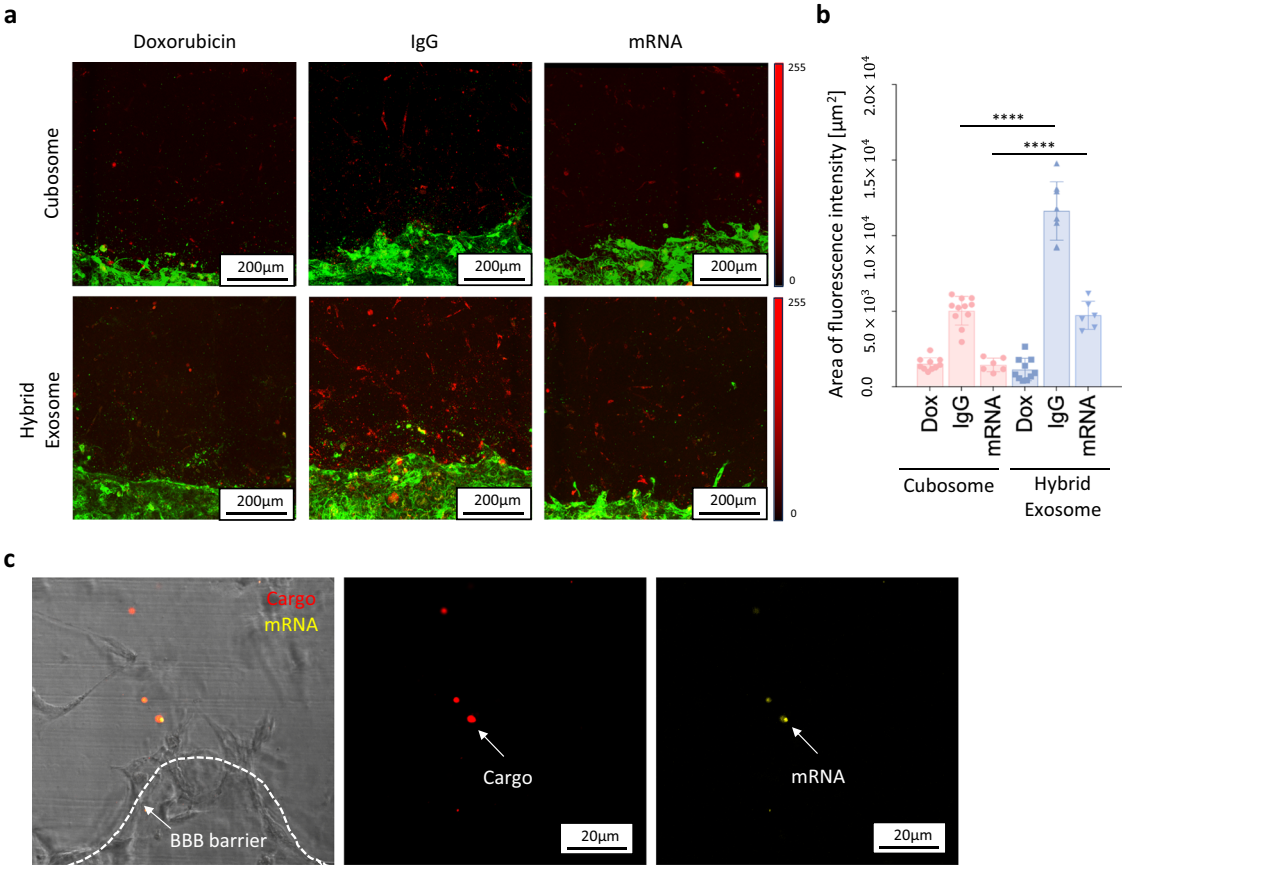

Fig. 7 | Biomedical application of hybrid exosomes for drug delivery across the BBB. a Confocal microscopy images showing the permeability of doxorubicin, IgG, and mRNA when delivered via cubosomes (top) and hybrid exosomes (bottom) across the BBB model. Scale bar: 200 μm. **b** Quantitative analysis of the area of fluorescence intensity for doxorubicin (Dox), IgG, and mRNA delivered using cubosomes and hybrid exosomes. Hybrid exosomes significantly enhance the transport of IgG and mRNA across the BBB compared to cubosomes. Data are presented as mean values with SD. Statistical significance: ****$p < 0.0001$ (mRNA: $n = 6$, Dox and IgG: $n > 8$; n represents the number of independent experiments). Statistical significance was determined using an ordinary one-way ANOVA followed by Tukey's multiple comparisons test,. **c** Confirmation of intact mRNA transport across the BBB. Texas Red-labeled hybrid exosomes (red) successfully encapsulate and deliver mRNA (yellow) across the endothelial barrier. The merged image shows the colocalization of hybrid exosomes and mRNA beyond the BBB boundary. Scale bar: 20 μm.

in fluorescence intensity and absorbance intensity using an ELISA kit, respectively.

Exosome isolation

Exosome was isolated from Hela, MDA-MB-231, and HBMEC cell media using the ExoQuick kit based on non-solvent precipitation. For labeling, DiI dye was added to the exosome pellet at the same volume and incubated at 37 °C for 20 min. Subsequently, the exosomes were spun down to remove free dye and washed three times. The exosomes were then prepared at various concentrations (cubosome:exosome = 1:1, 1:10) based on a size close to 100 nm as determined by dynamic light scattering (DLS).

Kinetics of fusion

To confirm the fusion process through the FRET experiment, 0.5% NBD-PE and Liss Rod-PE were added respectively to the cubosome. Cubosomes and exosomes number concentration was determined through DLS measurements. As shown in Supplementary Fig. 4a, the increase in fusion rate became saturated above a cubosome-to-exosome ratio of 1:5 in PBS. Therefore, to clearly observe the differences in fusion kinetics based on the cubosome-to-exosome ratios, the number ratios of 1:1 and 1:10 were chosen for this study. Subsequently, they were mixed at room temperature through pipetting. As the distance between the NBD-PE and the Liss Rhod-PE increased, the energy transfer of NBD-PE decreased. Therefore, the intensity of the Liss Rhod-PE decreased, and the intensity change was measured at 10 s intervals for 10 min. Additionally, SAXS was measured at 60 s intervals for 10 min to observe the first peak intensity change of the cubic phase. Subsequently, to only consider the structure factor, the background signal was subtracted by scattering from capillary filled with deionized water and polynomial background. And the fusion process was confirmed through Cryo-TEM.

Fusogenicity of cubosome

The free energy of membrane can be described using the Helfrich equation (F/A: Free energy per area, C: mean curvature, C_0: spontaneous curvature, $\bar{\kappa}$: Gaussian modulus, K: Gaussian curvature ($K = C_1C_2$)):

$$F/A = k/2(C - C_0)^2 + \bar{\kappa}K \quad (4)$$

The first term describes the free energy cost of bending a membrane away from C_0. Since we only consider the equilibrium, we can only consider the second term which describes the contribution of the membrane's Gaussian curvature. Based on this, we can calculate the total free energy of the individual lipid nanoparticles using Gauss-Bonnet theorem (g represents topological genus, or number of holes

in simpler term). The result is follows:

$$F = \bar{\kappa} \int K dA = 4\pi\bar{\kappa}(1-g) \quad (5)$$

If we consider the free energy change upon fusion (assume it generates one hole upon fusion; g = 1 for fused structure), we can describe free energy change as:

$$\Delta F_{\text{fusion}} = F_{\text{fused}} - F_{cubo} - F_{exo} = -4\pi(\bar{\kappa_{cubo}} + \bar{\kappa_{exo}}) \quad (6)$$

Since $\bar{\kappa}$ is positive and its absolute value is higher than exosome (where $\bar{\kappa_{exo}}<0$) in most cases, free energy change becomes negative. This means cubosome spontaneously fuse with exosome, forming a fused structure.

Drug loading in exosomes

The drug lost while fusion was removed in the same way as free-drug removal when drug loading on the cubosome. The drug loading efficiency was calculated as follows:

$$DE(\%) = \frac{intensity\ or\ amount\ of\ drug\ in\ fusion\ solution}{intensity\ or\ amount\ of\ drug\ in\ cubosome\ solution} \quad (7)$$

Cryogenic transmission electron microscopy (Cryo-TEM)

We used Cryo-TEM (FEI Tecnai F20 G2 at 200 kV) to check cubosome and the process of fusion. 2–3 μl samples were applied to the grid (Structure Probe Incorporation, PA, USA) with a blotting time of 3 s (Vitrobot FP5350/60). And the grid was quickly dropped into liquid ethane. The prepared sample was transferred to a Cryo-TEM instrument while maintaining −170 °C.

Small-angle X-ray scattering (SAXS)

Small-Angle X-ray Scattering (SAXS). Synchrotron SAXS was carried out on Pohang Accelerator Laboratory Beamline 3 C. The sample-to-detector distance was 1 m with a q-range from 0.03 to 0.16 $Å^{-1}$. All the samples were prepared in a DW-dispersed state, and measured at 25 °C after equilibrium with exposure time of 10 sec. The synchrotron X-ray source had an average photon energy of 16.9 keV with an average beam size of 60 μm × 600 μm (V × H). The scattered photons were recorded by using an Eiger X4M detector (Dectris, Switzerland) and 2D X-ray diffraction images were integrated using the custom software provided by the beamline 3 C. mRNA loaded cubosomes were analyzed by custom-built lab SAXS. The sample-to-detector distance was 1.55m and the X-ray source has an average photon energy of 8.0478 keV with a beam size (FWHM) of 1000 μm × 1000 μm (H × V). 2D scattering data were radially averaged via Fit2D software upon acquisition on an Eiger 1 M detector (Dectris, Switzerland). The data were plotted after measuring deionized water under the same conditions to remove the background.

DLS

The sample size, polydispersity index (PDI), and number concentration were determined using a dynamic light scattering (Zetasizer Ultra Red Label, Malvern, UK). The data presented correspond to the average of three consecutive measurements.

Fluorescence microscopy

All samples were measured at 64X for 1 s. In the experiment of loading mRNA into cubosomes, the mRNA was stained with a FAM-tagged primer, and the cubosomes were stained with Texas Red. The mRNA-loaded cubosomes were prepared by diluting them to 0.5X. In the experiment confirming the fusion of cubosomes and exosomes, the cubosomes were stained with NBD-PE, and the exosomes were stained with DiI. And they were diluted to 0.1X.

Cell culture

Human Brain Microvascular Endothelial Cells (HBMECs; Cat. No. 1000, Lot No. 609.01.02.01.02, CellSystems, USA) and Human Astrocytes (HA; Cat. No. 1800, Lot No. 33655, ScienCell, USA) were cultured in endothelial cell medium (ECM; Cat. No. 1001, ScienCell, USA), and astrocyte medium (AM; Cat. No. 1801, ScienCell, USA), respectively, and used in the experiment at passages 4 and 5. Human Brain Vascular Pericytes (HBVP; Cat. No. 1200, Lot No. 34237, ScienCell, USA) were cultured in pericyte medium (PM; Cat. No. 1201, ScienCell, USA), and used in the experiment at passages 6 and 7. The cells were maintained in an incubator at 37 °C, with above 95% humidity and 5% CO_2, following the manufacturer's recommended protocol.

Hydrogel preparation for 3D cell culture

The fibrinogen from bovine plasma (Cat. No. F8630, Sigma-Aldrich, USA) was dissolved in phosphate-buffered saline (PBS; Cat. No. 17–516Q, Lonza, Switzerland) at a concentration of 12 mg/ml. Aprotinin was also dissolved in PBS, and incubated for 30 min. Both solutions were filtered through a 0.2 μm filter to remove any clots. The fibrinogen solution was then mixed with the aprotinin solution in a volume ratio of 25:4. This mixed hydrogel solution was combined with the cell suspension at a volume ratio of 1:3, resulting in a final fibrin gel concentration of 2.5 mg/ml. Separately, the thrombin solution was prepared by dissolving thrombin (Cat. No. T4648, Sigma-Aldrich, USA) in PBS at a concentration of 50 U/ml. After incubating for 30 min and filtering according to the manufacturer's recommendations, this acellular hydrogel solution was then mixed with the thrombin solution at a volume ratio of 50:1, resulting in gelation within approximately 5 min.

Construction of in vitro BBB model

To construct the in vitro BBB model, both HA and HBVP cells were prepared as suspensions at a concentration of 2×10^6 cells/mL. These cells were mixed in a 6:1 ratio, taking into account their respective growth rates. This cell mixture was then combined with fibrin hydrogel solution and thrombin, as previously described. The mixture was injected into the channels of the microfluidic device using an automatic micropipette, which facilitated the introduction of as much acellular hydrogel as possible before gelation occurred. The device was then incubated for 5 min to allow the hydrogel to harden. Following this, HBMEC cells were prepared at a concentration of 2×10^6 cells per mL^{-1}. A 3 μl suspension of HBMEC cells was introduced into one side channel of the device. The device was tilted 90 degrees to ensure even attachment of the HBMEC cells to the fibrin hydrogel wall. After 15 min to allow for cell attachment, the other side channel was filled with culture medium. The co-culture medium was prepared by adding astrocyte growth supplement (Cat. No. 1852, ScienCell, USA) and pericyte growth factor (Cat. No. 1252, ScienCell, USA) to the HBMEC culture medium. The medium was changed daily, and cells were cultured for a total of 4 days.

Sample preparation for in vitro BBB model

To examine the uptake and transport trends of particles in the in vitro BBB model, cubosomes and exosomes were labeled with Texas Red and DiI, respectively. The cubosome solution was diluted 5000-fold in distilled water(DW), and the average number concentration was determined through DLS measurements (average concentration: 7.30×10^{12} particles/mL). Exosomes and hybrid exosomes were prepared based on the number concentration of cubosomes. Pure exosome samples were prepared at the same number concentration as the cubosomes, while hybrid exosomes were prepared at cubosome-to-exosome number ratios of 1:0.1 and 1:10.

In experiments to evaluate the BBB transport of drug-loaded carriers, the carriers themselves were not labeled. Instead, the transport of drugs within the carriers was confirmed using the intrinsic fluorescence properties of doxorubicin (DOX), fluorescently tagged IgG (red), and Cy5-labeled mRNA (red). Additionally, to observe the co-localization of the drugs and the carriers, hybrid exosomes and mRNA were prepared by labeling them with Texas Red (red) and FAM (green), respectively, and hybrid exosomes were prepared at cubosome-to-exosome number ratios of 1:0.1.

Imaging the transport of hybrid drug carriers across BBB

Once the BBB was fully mature, the medium was aspirated from each reservoir. For each reservoir, 120 μL of co-culture medium containing various drug carriers (i.e cubosome, exosome, or hybrid exosome-fused cubosome) and fluorescein-labeled Ulex europaeus agglutinin (FL-1061, Vector Laboratories, USA) was prepared. The Ulex europaeus agglutinin was diluted at a ratio of 1:1000 according to the manufacturer's instructions and used to label the endothelium. This solution was then infused into the endothelium channel to measure the transport across the BBB of each drug component. The opposite side of the channel was filled with 100 μL of co-culture medium. After a 6-h incubation period, both reservoirs were replaced with fresh co-culture medium, and the samples were ready for imaging. Confocal images were obtained using an inverted confocal laser scanning microscope (LSM 800, Carl Zeiss, Germany) equipped with 10× and 20× objective lenses. The microscope was also equipped with a live-cell imaging system that maintains living cells in a healthy condition, including temperature, atmosphere, humidity, osmolarity, and pH. The microscope was operated using Zeiss ZEN software. Image resolution was approximately 3.2 pixels per μm without binning. For three-dimensional imaging, sections approximately 100 μm thick were imaged from the bottom to the top of the endothelium using sequential z-stacks set 3 μm apart.

Immunocytochemistry

The samples were fixed with 4% (w/v) paraformaldehyde (Biosesang, Korea) for 30 min and then permeabilized with 0.2% Triton X-100 (Sigma-Aldrich, USA) for 15 min. For endothelial cell (EC) markers, we used Alexa Fluor 488-conjugated anti-human cluster of differentiation 31 (CD31; 1:1200; Cat. No. 303110, Biolegend, USA) and DyLight 488-conjugated Ulex europaeus agglutinin I (Lectin; 1:1000; Cat. No. FL-1061, Vector, UK). Alexa Fluor 594-conjugated anti-human alpha-smooth muscle actin (α-SMA; 1:200; Cat. No. IC1420T, R&D Systems, USA) was employed as a pericyte marker, while Alexa Fluor 647-conjugated glial fibrillary acidic protein (GFAP; 1:200; Cat. No. 560298, BD Bioscience, USA) was used to label astrocytes. For tight junction protein markers, we used ZO-1 monoclonal antibody conjugated with Alexa Fluor 594 (1:200; Cat. No. 339194, Invitrogen, USA), Claudin-5 monoclonal antibody conjugated with Alexa Fluor 488 (1:200; Cat. No. 352588, Invitrogen, USA), and VE-cadherin conjugated with Alexa Fluor 488 (1:200; Cat. No. 53-1441-82, Invitrogen, USA). All antibodies were used at a dilution of 1:200, and all immunofluorescence markers were diluted in bovine serum albumin (BSA, Cat. No. A0100-010, GenDEPOT, USA)-containing PBS to minimize non-specific binding. The samples were maintained in PBS and stored at 4 °C until imaging.

To label human astrocytes for long-term tracking, we utilized the Qtracker™ 565 Cell Labeling Kit (Cat. No. Q25031MP, Invitrogen, USA) and followed the manufacturer's instructions. To prepare an approximately 2 nM labeling solution, 25 μL of Qtracker® nanocrystals (Component A) and 25 μL of Qtracker® carrier (Component B) were pre-mixed in a 1.5 mL microcentrifuge tube and incubated at room temperature for 5 min. After incubation, approximately 5 mL of fresh complete growth medium was added to the tube, followed by vortexing for 30 s. The prepared labeling medium was then added to a 100 mm culture dish containing astrocytes at 70% confluency, and the cells were incubated overnight for robust labeling.

Image analysis

Post-image processing, including maximum-intensity projection, orthogonal view, and 3D reconstruction, was performed using the ZEN software program (Carl Zeiss, Germany). Confocal image analysis was carried out using the open-access software Fiji (http://fiji.sc). Z-projection images were generated by applying the maximum intensity projection of acquired z-stack images. Pixel values were extracted to CSV files from confocal images, and these values were summed column by column. The resulting values were then averaged every 10 columns. While contrast enhancement was used to highlight the spatial distribution of transported hybrid carriers in representative images, the threshold was carefully set to prevent oversaturation, ensuring that intensity variations with distance remain distinguishable. To ensure consistency in quantification, a fixed threshold range was uniformly applied across all images. This approach minimizes bias and enables reliable comparisons of the spatial distribution of transported hybrid carriers.

Statistics and reproducibility

For cryogenic transmission electron microscopy (Cryo-TEM) and Fluorescence Microscopy data, statistical analyses were performed on pooled data from at least 3 independent experiments.

For imaging the transport of hybrid drug carriers across the BBB, each experiment was conducted on a single chip containing 28 independent samples, enabling high-throughput screening without the need for repeated confocal imaging of the same sample. The chip was typically divided into three experimental conditions, with 10, 10, and 8 samples, respectively, ensuring independent biological replicates across conditions. Imaging was performed accordingly, maintaining consistency in data collection.

Statistical analyses were conducted using GraphPad Prism software. An ordinary one-way ANOVA followed by Tukey's multiple comparisons test was used to determine statistical significance. The p-value thresholds were set as follows: $^{*}p < 0.05$, $^{**}p < 0.01$, $^{***}p < 0.001$, $^{****}p < 0.0001$, and ns (not significant). Error bars represent the standard deviation (SD).

Reporting summary

Further information on research design is available in the Nature Portfolio Reporting Summary linked to this article.

Data availability

All data from this study can be found in the main text and Supplementary Information. Additionally, the source data for Figs. 1–7, Supplementary Figs. 1–6, and supplementary Data 1, 2 are provided in the Source Data File along with the main text. Source data are provided with this paper.

References

1. Zhang, Y., Liu, Y., Liu, H. & Tang, W. H. Exosomes: biogenesis, biologic function and clinical potential. *Cell Biosci.* **9**, 19 (2019).
2. Doyle, L. M. & Wang, M. Z. Overview of extracellular vesicles, their origin, composition, purpose, and methods for exosome isolation and analysis. *Cells* **8**, 727 (2019).
3. Kim, H. I. et al. Recent advances in extracellular vesicles for therapeutic cargo delivery. *Exp. Mol. Med.* **56**, 836–849 (2024).
4. Herrmann, I. K., Wood, M. J. A. & Fuhrmann, G. Extracellular vesicles as a next-generation drug delivery platform. *Nat. Nanotechnol.* **16**, 748–759 (2021).
5. Bang, S. et al. Exosome-inspired lipid nanoparticles for enhanced tissue penetration. *ACS Nano* **19**, 8882–8894 (2025).

6. Chakraborty, S. et al. How cholesterol stiffens unsaturated lipid membranes. *Proc. Natl. Acad. Sci. USA.* **117**, 21896–21905 (2020).
7. Donoso-Quezada, J., Ayala-Mar, S. & González-Valdez, J. The role of lipids in exosome biology and intercellular communication: Function, analytics and applications. *Traffic* **22**, 204–220 (2021).
8. Usman, W. M. et al. Efficient RNA drug delivery using red blood cell extracellular vesicles. *Nat. Commun.* **9**, 2359 (2018).
9. Butreddy, A., Kommineni, N. & Dudhipala, N. Exosomes as naturally occurring vehicles for delivery of biopharmaceuticals: Insights from drug delivery to clinical perspectives. *Nanomaterials* **11**, 1481 (2021).
10. Sato, Y. T. et al. Engineering hybrid exosomes by membrane fusion with liposomes. *Sci. Rep.* **6**, 21933 (2016).
11. Piffoux, M., Silva, A. K. A., Wilhelm, C., Gazeau, F. & Tareste, D. Modification of extracellular vesicles by fusion with liposomes for the design of personalized biogenic drug delivery systems. *ACS Nano* **12**, 6830–6842 (2018).
12. Lin, Y. et al. Exosome-liposome hybrid nanoparticles deliver CRISPR/Cas9 system in MSCs. *Adv. Sci.* **5**, 1700611 (2018).
13. Chen, M. et al. Injectable microgels with hybrid exosomes of chondrocyte-targeted FGF18 gene-editing and self-renewable lubrication for osteoarthritis therapy. *Adv. Mater.* **36**, e2312559 (2024).
14. Malle, M. G. et al. Programmable RNA loading of extracellular vesicles with toehold-release purification. *J. Am. Chem. Soc.* **146**, 12410–12422 (2024).
15. Gao, C. et al. Injectable immunotherapeutic hydrogel containing RNA-loaded lipid nanoparticles reshapes tumor microenvironment for pancreatic cancer therapy. *Nano Lett.* **22**, 8801–8809 (2022).
16. Duskunovic, N., Im, S. H., Lee, J. & Chung, H. J. Effective mRNA delivery by condensation with cationic nanogels incorporated into liposomes. *Mol. Pharm.* **20**, 3088–3099 (2023).
17. Wu, S. et al. Therapeutic m6A eraser ALKBH5 mRNA-loaded exosome-liposome hybrid nanoparticles inhibit progression of colorectal cancer in preclinical tumor models. *ACS Nano* **17**, 11838–11854 (2023).
18. Zhang, J. et al. Highly effective detection of exosomal miRNAs in plasma using liposome-mediated transfon CRISPR/Cas13a. *ACS Sens* **8**, 565–575 (2023).
19. Lv, H., Zhang, S., Wang, B., Cui, S. & Yan, J. Toxicity of cationic lipids and cationic polymers in gene delivery. *J. Control. Release* **114**, 100–109 (2006).
20. Kedmi, R., Ben-Arie, N. & Peer, D. The systemic toxicity of positively charged lipid nanoparticles and the role of Toll-like receptor 4 in immune activation. *Biomaterials* **31**, 6867–6875 (2010).
21. Luzzati, V., Tardieu, A. & Gulik-Krzywicki, T. Polymorphism of lipids. *Nature* **217**, 1028–1030 (1968).
22. Zheng, L., Bandara, S. R., Tan, Z. & Leal, C. Lipid nanoparticle topology regulates endosomal escape and delivery of RNA to the cytoplasm. *Proc. Natl. Acad. Sci. USA.* **120**, e2301067120 (2023).
23. Leal, C., Bouxsein, N. F., Ewert, K. K. & Safinya, C. R. Highly efficient gene silencing activity of siRNA embedded in a nanostructured gyroid cubic lipid matrix. *J. Am. Chem. Soc.* **132**, 16841–16847 (2010).
24. Helfrich, W. Elastic properties of lipid bilayers: theory and possible experiments. *Z. Naturforsch. C* **28**, 693–703 (1973).
25. Kim, H. & Leal, C. Cuboplexes: Topologically active siRNA delivery. *ACS Nano* **9**, 10214–10226 (2015).
26. Kim, H., Song, Z. & Leal, C. Super-swelled lyotropic single crystals. *Proc. Natl. Acad. Sci. USA.* **114**, 10834–10839 (2017).
27. Ding, C. et al. Cellular delivery of relaxin-2 mRNA as a potential treatment for kidney fibrosis. *Mater. Today Bio* **21**, 100716 (2023).
28. Kim, H., Sung, J., Chang, Y., Alfeche, A. & Leal, C. Microfluidics synthesis of gene silencing cubosomes. *ACS Nano* **12**, 9196–9205 (2018).
29. Dammes, N. et al. Conformation-sensitive targeting of lipid nanoparticles for RNA therapeutics. *Nat. Nanotechnol.* **16**, 1030–1038 (2021).
30. Wang, C., Zhao, C., Wang, W., Liu, X. & Deng, H. Biomimetic non-cationic lipid nanoparticles for mRNA delivery. *Proc. Natl. Acad. Sci. USA.* **120**, e2311276120 (2023).
31. Jahn, A. et al. Microfluidic mixing and the formation of nanoscale lipid vesicles. *ACS Nano* **4**, 2077–2087 (2010).
32. Maeki, M. et al. Understanding the formation mechanism of lipid nanoparticles in microfluidic devices with chaotic micromixers. *PLoS One* **12**, e0187962 (2017).
33. Pilkington, C. P. et al. A microfluidic platform for the controlled synthesis of architecturally complex liquid crystalline nanoparticles. *Sci. Rep.* **13**, 12684 (2023).
34. Liu, H. et al. Beyond the endosomal bottleneck: Understanding the efficiency of mRNA/LNP delivery. *Adv. Funct. Mater.* **34**, 2404510 (2024).
35. Koltover, I., Salditt, T., Rädler, J. O. & Safinya, C. R. An inverted hexagonal phase of cationic liposome-DNA complexes related to DNA release and delivery. *Science* **281**, 78–81 (1998).
36. Structure of DNA-Cationic Liposome Complexes. DNA Interaction in Multilamellar Membranes in Distinct Interhelical Packing Regimes. *Science* **275**, 810–814 (1997).
37. Marušič, N. et al. Increased efficiency of charge-mediated fusion in polymer/lipid hybrid membranes. *Proc. Natl. Acad. Sci. USA.* **119**, e2122468119 (2022).
38. Dyett, B. P., Yu, H., Strachan, J., Drummond, C. J. & Conn, C. E. Fusion dynamics of cubosome nanocarriers with model cell membranes. *Nat. Commun.* **10**, 4492 (2019).
39. Goldberger, M. L. & Watson, K. M. *Collision Theory*. (Dover Publications, Mineola, NY, 2004).
40. Lira, R. B., Robinson, T., Dimova, R. & Riske, K. A. Highly efficient protein-free membrane fusion: A giant vesicle study. *Biophys. J.* **116**, 79–91 (2019).
41. Cavalcanti, R. R. M., Lira, R. B. & Riske, K. A. Membrane fusion biophysical analysis of fusogenic liposomes. *Langmuir* **38**, 10430–10441 (2022).
42. Yu, J. et al. Perfusable micro-vascularized 3D tissue array for high-throughput vascular phenotypic screening. *Nano Converg* **9**, 16 (2022).
43. Nance, E., Pun, S. H., Saigal, R. & Sellers, D. L. Drug delivery to the central nervous system. *Nat. Rev. Mater.* **7**, 314–331 (2022).

Acknowledgements

This work was supported by the National Research Foundation of Korea (NRF) grant funded by the Korea government (MSIT) (No. RS-2023-00209955, Participant: G.S., J.C.P., H.K). This research was partially supported by the Korea Institute of Science and Technology (KIST) (2E33111, Participant: G.S., J.C.P., H.K and 2E33712, Participant: J.S., H.N.K.). This work was also supported by Korea Institute of Planning and Evaluation for Technology in Food, Agriculture and Forestry (IPET) through High-Risk Animal infectious Disease Control Technology Development Program, funded by Ministry of Agriculture, Food and Rural Affairs (MAFRA)(RS-2024-00396818, Participant: G.S., J.C.P., H.K). This was also supported by the National Research Foundation (NRF) grant funded by the korea government (MSIT) (RS-2024-00424551, RS-2024-00395393, Participant: J.S., H.N.K.). Enparticle kindly provided microfluidic mixer for cubosome fabrication. Professor Jeung Sang Go at Pusan National University provided valuable feedback on choosing flow parameters. We gratefully acknowledge Professor Noo Li Jeon at Seoul National University for generously providing the BBB chips used in this study. We appreciate Dr. Youli Li for the insightful comments on X-ray scattering analysis. Cartoons in Figs. 1b, 5a, 6f were created with BioRender.com.

Author contributions

H.K. proposed the idea. H.K. and J.C.P. conceptualize the idea. G.S. designed and performed the overall experiments, analyzed the data under the supervision of H.K.; G.S. prepared samples for in vitro BBB experiments; J.S. designed and performed in vitro BBB experiments; H.N.K. provided experimental guidance for the BBB experiments.; H.N.K. and H.K. provided funding support; G.S., J.S., H.N.K. and H.K wrote the manuscript. All authors commented on the manuscript.

Competing interests

The Korea Institute of Science and Technology is in the process of applying for a Korean invention patent (10-2025-0058245) related to the subject matter of this paper.

Additional information

Supplementary information The online version contains supplementary material available at https://doi.org/10.1038/s41467-025-59489-5.

Correspondence and requests for materials should be addressed to Hong Nam Kim or Hojun Kim.

Peer review information *Nature Communications* thanks the anonymous reviewers for their contribution to the peer review of this work. A peer review file is available.